Please cite this paper as

Hu S, Zhu S, Alam M S, and Wang W (2021) Machine Learning-aided Peak and Residual Displacement-based Design Method for Enhancing Seismic Performance of Steel Moment-resisting Frames by Installing Self-centering Braces. Engineering Structures. 271: 114935. https://doi.org/10.1016/j.engstruct.2022.114935

Machine learning-aided peak and residual displacement-based design method for enhancing seismic performance of steel moment-resisting frames by installing self-centering braces

Shuling Hu[a,b], Songye Zhu[a,*], M. Shahria Alam[b], Wei Wang[c]

[a] *Dept. of Civil and Environmental Engineering, The Hong Kong Polytechnic University, Kowloon, Hong Kong, China.*
[b] *School of Engineering, The University of British Columbia, Kelowna, BC V1V 1V7, Canada.*
[c] *State Key Laboratory of Disaster Reduction in Civil Engineering & Department of Structural Engineering, Tongji University, Shanghai 200092, China.*

ABSTRACT:

Conventional steel moment-resisting frames (SMRFs) absorb seismic energy through steel yielding behavior, leading to significant residual displacement. Although steel yielding behavior can ensure the seismic safety of SMRFs under strong earthquakes, excessive residual displacement may lead to post-earthquake demolition decisions, causing a large amount of economic loss. This paper aims to develop a peak and residual displacement-based design (PRDBD) method for controlling the peak and residual inter-story drift responses of SMRFs by installing self-centering braces. The peak and residual displacements are both set as the design targets in the proposed PRDBD method. To this end, the machine learning prediction models of inelastic and residual displacement ratios were first developed based on the median responses of single-degree-of-freedom systems under earthquakes. The detailed design steps of the proposed PRDBD method were subsequently introduced. The three- and nine-story demonstration buildings were retrofitted by using the PRDBD method with two different design targets. Static and dynamic analyses were conducted to validate the efficiency of the proposed PRDBD method. The static analysis results indicated that the self-centering braces could efficiently enhance the SMRF's stiffness and strength. The retrofitted SMRFs showed no strength deterioration, whereas the original SMRFs showed obvious strength deterioration at the roof drifts of 3.2% and 2.5% in the three- and nine-story buildings, respectively. The dynamic analysis results confirm that the self-centering braces can efficiently reduce the

[*] *Corresponding author: Professor, Department of Civil and Environment Engineering, The Hong Kong Polytechnic University, Hung Hom, Kowloon, Hong Kong, E-mail: songye.zhu@polyu.edu.hk.*

peak and residual inter-story drift responses of the existing SMRFs and the retrofitted SMRFs can achieve the peak and residual inter-story performance objectives under the considered seismic intensity. Moreover, the retrofitted SMRFs can be fully recoverable after maximum considered earthquakes by controlling the maximum residual inter-story drift lower than 0.2%.

KEYWORDS: Peak and residual displacement; Machine learning; Residual displacement-based design method; Post-earthquake repairability; Moment-resisting frames; Self-centering brace.

Highlights:

1. Machine learning prediction models of C_μ and C_r were developed for the RSMRF.

2. A peak and residual displacement-based design method was developed for retrofitting SMRFs.

3. The designed RSMRFs can achieve the desired peak and residual inter-story drift responses.

4. The designed RSMRFs have no repair requirements after MCE excitations.

1. INTRODUCTION

Due to architectural aesthetics and versatile advantages, conventional steel moment-resisting frames (SMRFs) are widely used in building structures. Moreover, the highly ductile behavior of SMRFs offers a reliable capacity to withstand large plastic displacement without significant strength deterioration and instability and thus SMRFs can ensure seismic safety under strong earthquakes, but it also leads to significant residual inter-story drifts. The 2011 Christchurch earthquake indicates that the building structures with large residual inter-story drifts are extremely difficult, if not impossible, to repair [1, 2]. Based on the investigation by McCormick et al. [3], it is a better and more economic choice to demolish and rebuild than repair the buildings with a maximum residual inter-story drift larger than 0.5%. Nevertheless, the past studies [4, 5] confirm that the residual inter-story drifts of SMRFs are usually larger than 0.5% under design basis earthquakes (DBE) or maximum considered earthquakes (MCE). It is noteworthy that nonstructural damage may lead to more seismic loss and business disruption than structural damage for buildings under earthquakes [6-9]. However, the nonstructural damage control is beyond the scope of the presented study, and this paper will be focused on structural damage mitigation by controlling peak and residual inter-story drift responses of SMRFs.

Inspired by the precast concrete structural systems [10], the unbonded post-tensioning techniques were introduced to develop self-centering steel beam-to-column connections to reduce residual inter-story drift responses of SMRFs under strong earthquakes. Ricles et al. [11] and Garlock et al. [12] developed the post-tensioned beam-to-column connections (denoted as PT connections) with steel angles to eliminate the residual deformation of conventional steel beam-to-column connections. The PT strands and steel angles were included in the PT connections to achieve self-centering behavior and energy-absorbing capacity.

Past experimental and numerical studies have extensively validated the efficiency of the PT connections in controlling residual inter-story drift responses of SMRFs [11, 12]. However, the PT connections introduce an opening/closing gap between beams and columns under earthquakes, leading to severe floor damage [13]. The following significant efforts have been made to address the gap opening issue by introducing different configurations of self-centering beam-to-column connections [13, 14]. In addition to the self-centering beam-to-column connections, many other self-centering solutions, including self-centering walls [15-17], self-centering rocking structures [4, 18-23], self-centering braces [24-30], etc., have been widely investigated. Among these self-centering technologies, self-centering braces represent one of the efficient solutions to reduce the residual inter-story drift responses of SMRFs. Moreover, axial deformation of self-centering braces does not introduce damage to the floor slabs, and self-centering braces can provide sufficient stiffness to control the lateral displacement of SMRFs. Accordingly, different types of self-centering braces have been used to enhance the seismic performance of SMRFs [31-35]. For example, Ozbulut et al. [34] upgraded SMRFs using self-centering viscous dampers to reduce the peak and residual inter-story drifts and peak floor acceleration responses; Qiu et al. [35] reduced the maximum and residual inter-story drift responses of SMRFs by installing shape memory alloy braces; Zhu et al. [32] investigated the seismic performance of steel moment-resisting frames with self-centering viscous-hysteretic devices; and Chou et al. [31] tested the steel buildings with self-centering braces. These past investigations have confirmed the efficiency of self-centering braces in enhancing the seismic performance of SMRFs by reducing the peak and residual inter-story drift responses. Nevertheless, how to rationally design the self-centering braces to make the upgraded SMRFs achieve both desired maximum and residual inter-story drift targets remains an unanswered question.

The major contribution of this paper is developing a new peak and residual displacement-based design (PRDBD) method, which can control both the peak and residual inter-story drift responses of SMRFs to the desired levels by installing self-centering braces. The peak and residual displacements are both set as the design targets in the proposed PRDBD method. To this end, the machine learning prediction models of inelastic and residual displacement ratios were first developed based on the median responses of single-degree-of-freedom (SDOF) systems under earthquakes. The detailed design steps of the proposed PRDBD method were subsequently introduced. The three- and nine-story demonstration buildings were retrofitted by using the PRDBD method with two different design targets. Static and dynamic analyses were conducted for the retrofitted SMRF (denoted as RSMRF) to validate the efficiency of the proposed PRDBD method.

2. Inelastic and residual displacement ratio of RSMRF

The proposed PRDBD method was developed based on the constant-ductility inelastic displacement ratio (i.e., C_μ) and residual displacement ratio (i.e., C_r) of RSMRF. The prediction models of C_μ and C_r were developed based on the nonlinear dynamic analysis of the SDOF system. Specifically, the values of C_μ and C_r are usually related to the structural period T, ductility ratio μ, and hysteretic parameters of RSRMF.

Various types of self-centering braces were developed in previous investigations [28-30, 36-39]. The self-centering brace developed by Wang et al. [40] was adopted in this paper to retrofit the existing SMRFs for demonstration (see Fig. 1(a)). As shown in Fig. 1(a), the friction plate and the disc spring provide the energy-dissipation and self-centering capacities, respectively, in the considered self-centering brace. The past experimental investigations [40] confirmed that the considered self-centering brace could achieve the desired flag-shaped hysteretic behavior. Accordingly, the hysteretic responses of RSMRF can be obtained by placing the hysteretic responses of SMRF and the self-centering brace in parallel, as shown in Figs. 1(b) and 1(c). The bilinear elastoplastic hysteretic model and flag-shaped hysteretic model were used in this paper to describe the hysteretic behavior of the SMRF and self-centering brace, respectively. The ratio of the post-yield stiffness to the initial stiffness of SMRF is defined as α_1, and that of the self-centering brace is defined as α_2. The energy-absorbing capacity of the self-centering brace is described using the energy-dissipation factor β. As shown in Fig. 1(c), the self-centering brace with larger β values will achieve better hysteretic energy-dissipation capacity. The initial stiffness ratio of SMRF to RSMRF is defined as:

$$\eta = \frac{k_1}{k_0} \tag{1}$$

where k_0 and k_1 are the initial stiffness of RSMRF and SMRF, respectively. Accordingly, the initial lateral stiffness provided by self-centering brace k_2 can be obtained as:

$$k_2 = (1-\eta)k_0 \tag{2}$$

The strength ratio of the self-centering brace to SMRF is defined as:

$$\lambda = \frac{F_{y2}}{F_{y1}} \tag{3}$$

where F_{y1} and F_{y2} are the lateral yield strengths provided by SMRF and self-centering brace, respectively.

Fig. 2 shows the considered linear and nonlinear SDOF systems. Based on Fig. 2, the ductility ratio μ is defined as:

$$\mu = \frac{u_t}{u_{y1}} \tag{4}$$

where u_{y1} and u_t are the yield displacement of SMRF and the maximum displacement of the nonlinear SDOF system.

The strength reduction factor R is defined as:

$$R = \frac{F_e}{F_{y1}} \tag{5}$$

where F_{y1} and F_e are the yield strength of SMRF and the maximum force of the linear SDOF system that has the same period T as the nonlinear SDOF system representing the RSMRF.

The nonlinear displacement ratio C_μ is defined as:

$$C_\mu = \frac{u_t}{u_e} \tag{6}$$

where u_e is the maximum displacement of the linear SDOF system.

The residual displacement ratio C_r is defined as:

$$C_r = \frac{u_r}{u_e} \tag{7}$$

where u_r is the residual displacement of the nonlinear SDOF system.

Dynamic analyses of the SDOF systems with various parameters were conducted to develop the prediction models of C_μ and C_r. Various parameter values are considered in this paper to cover the possible ranges of different design cases and capture the nonlinear relationships between the design parameters and C_μ/C_r. Fifteen fundamental period T ranging from 0.2 s to 3.0 s with 0.2 s step, five stiffness ratios of

SMRF to RSMRF, η = (0.1, 0.3, 0.5, 0.7, and 0.9), five strength ratios of self-centering brace to SMRF, λ = (0.1, 0.3, 0.5, 0.7, and 0.9), four ratios of post-yield stiffness to the initial stiffness of SMRF, α_1 = (0, 0.04, 0.08, and 0.12), six ratios of post-yield stiffness to the initial stiffness of self-centering brace, α_2 = (0, 0.04, 0.08, 0.12, 0.16, and 0.20), six energy-dissipation factors of self-centering brace, β = (0, 0.2, 0.4, 0.6, 0.8, and 1.0), and four ductility ratios, μ = (2, 4, 6, and 8), were considered in the dynamic analyses of SDOF systems. 32 far-field ground motions recommended in FEMA P-695 [41] were adopted in the dynamic analysis. Consequently, the values of C_μ and C_r can be calculated through the iterative dynamic analyses of SDOF systems with the specific values of T, η, λ, α_1, α_2, β, and μ. Based on the parametric dynamic analyses, 6,912,000 values of C_μ and C_r were obtained. This paper will focus on the median C_μ and C_r responses of the SDOF system under the considered 32 ground motions. Finally, 216,000 median values of C_μ and C_r were obtained with different combinations of the input parameters T, η, λ, α_1, α_2, β, and μ.

Benefiting from the excellent capacity in capturing the highly nonlinear relationship between the inputs and outputs, machine learning techniques have been widely used in earthquake engineering in recent research. Compared to the traditional empirical formula, the machine learning model can more accurately predict the structural responses under earthquakes [42]. Accordingly, the artificial neural network (ANN) algorithm was used in this paper to develop the prediction models of C_μ and C_r based on the parametric dynamic analysis results. According to the investigation by Friedman et al. [43], to avoid the overfitting of the developed prediction models, 70% of the database (i.e., 216,000 × 70% = 151,200 samples) were used as the training sets, and 30% of the database (i.e., 216,000 × 30% = 64,800 samples) were used as the testing sets. Because the training and testing sets are randomly selected, the evaluated accuracy of the obtained prediction models based on the testing dataset can represent the untrained dataset.

The coefficient of determination (R^2) and root mean squared error (RMSE) were used to evaluate the accuracy of the developed prediction models:

$$R^2 = 1 - \frac{\sum_{k=1}^{n_t} \left(\hat{y}_k - y_k \right)^2}{\sum_{k=1}^{n_t} \left(\hat{y}_k - \bar{y}_k \right)^2} \tag{8}$$

$$\mathrm{RMSE} = \sqrt{\frac{\sum_{k=1}^{n_t} \left(\hat{y}_k - y_k \right)^2}{n_t}} \tag{9}$$

where $\hat{y}_k$ and y_k are the prediction value and test value, respectively; $\bar{y}_k$ is the mean value of the test data; and n_t is the number of test data. Fig. 3 shows the performance of the ANN models for predicting C_μ and C_r. The values of R^2 for C_μ and C_r predicted by the ANN models are 0.9936 and 0.9512, respectively, and those of RMSE for C_μ and C_r are 0.0060 and 0.0052, respectively. The R^2 and RMSE values are close to 1.0 and 0, respectively, indicating the high accuracy of the developed ANN models for predicting C_μ and C_r.

Fig. 4 shows the comparison between the predicted values by the ANN models and actual values obtained from dynamic analyses for C_μ and C_r. As shown, the developed ANN models can efficiently capture the dynamic analysis results. To facilitate the application of the developed ANN models to the prediction C_μ and C_r of RSMRF, the software named ANNRSMRF-MEDIAN was developed based on the ANN models. The user interface of the ANNRSMRF-MEDIAN is shown in Fig. 5. The values of C_μ and C_r can be obtained by simply inputting the values of T, η, λ, α_1, α_2, β, and μ. This software is provided as the supplementary data of this paper.

4. PEAK AND RESIDUAL DISPLACEMENT-BASED DESIGN METHOD

Based on the developed prediction models of C_μ and C_r, the PRDBD method is proposed in this section for enhancing the seismic performance of existing SMRFs through the installation of self-centering braces. Fig. 6 shows the flowchart of the proposed design method, and the corresponding detailed design steps are described as follows:

1st step: The fundamental information of existing SMRF, including the floor mass (m_i), story elevation (h_i), structural layout, structural member size, and building location, can be obtained.

2nd step: The maximum and residual inter-story drifts of the existing SMRF can be evaluated through nonlinear dynamic analysis. If the maximum or residual inter-story drift responses are unsatisfactory, the following procedure can be used to design self-centering braces for enhancing the seismic performance of the existing SMRF.

3rd step: Determine the desired performance objectives by defining the target maximum inter-story drift ($\theta_{m,t}$) and target residual inter-story drift ($\theta_{r,t}$) under the considered seismic intensity (either DBE or MCE).

4th step: The yield base shear $V_{y,SMRF}$, post-yield stiffness ratio α_1, and yield inter-story drift $\theta_{y,SMRF}$ of the existing SMRF can be achieved through nonlinear pushover analysis. If the SMRF cannot obtain a uniform yield inter-story drift over the building height, $\theta_{y,SMRF}$ can be obtained as the average yield inter-story drift.

5th step: Based on the type and properties of the used self-centering braces, the hysteretic parameters (i.e., α_2 and β) can be determined.

6th step: Calculate the ductility ratio μ:

$$\mu = \frac{\Delta_t}{\Delta_y} \tag{10}$$

where Δ_t and Δ_y are the design displacement of the retrofitted SMRF (i.e., RSMRF) and the yield displacement of SMRF, respectively, and can be calculated as:

$$\Delta_t = \frac{\sum_{i=1}^{n}\left[m_i \Delta_{i,t}^{\ 2}\right]}{\sum_{i=1}^{n} m_i \Delta_{i,t}} \tag{11}$$

$$\Delta_y = \frac{\sum_{i=1}^{n}\left[m_i \Delta_{i,y}^{\ 2}\right]}{\sum_{i=1}^{n} m_i \Delta_{i,y}} \tag{12}$$

where $\Delta_{i,t}$ and $\Delta_{i,y}$ are the maximum and yield displacement of the i^{th} story. The lateral displacement profile developed by Karavasilis et al. [44] for SMRF was used in this paper. Accordingly, $\Delta_{i,t}$ and $\Delta_{i,y}$ can be calculated as:

$$\Delta_{i,t} = P_1 \theta_{m,t} h_i (1 - P_2 \frac{h_i}{H}) \tag{13}$$

$$\Delta_{i,y} = P_1 \theta_{y,\mathrm{SMRF}} h_i (1 - P_2 \frac{h_i}{H}) \tag{14}$$

where P_1 and P_2 are related to the story number and the ratio of column's strength to beam's strength (a_{cd}). Table 1 shows the values of P_1 and P_2. a_{cd} can be calculated as:

$$a_{cd} = \frac{\sum M_{Rc}}{\sum M_{Rb}} \tag{15}$$

where $\sum M_{Rc}$ and $\sum M_{Rb}$ are the sum of the plastic moment of resistance of columns and beams framing the joint.

7th step: Determine the initial values of η and λ. The fundamental period of RSMRF can be estimated as:

$$T_n = \frac{2\pi}{\omega_n} \tag{16}$$

$$\omega_n = \sqrt{\eta} \times \omega_{n,\mathrm{SMRF}} \tag{17}$$

where $\omega_{\mathrm{n,SMRF}}$ is the natural frequency of the existing SMRF. Then corresponding C_μ can be obtained through the developed ANN model.

8th step: Calculate the target inelastic displacement ratio $C_{\mu,t}$:

$$C_{\mu,t} = \frac{\Delta_t}{\Delta_e} \tag{18}$$

$$\Delta_e = S_d(T_n) \tag{19}$$

where $S_d(T_n)$ is the elastic design spectral displacement at T_n under considered seismic intensity (e.g., DBE or MCE).

9th step: The desired yield base shear of SMRF can be calculated as:

$$V_{\mathrm{SMRF},d} = \frac{WS_a(T_n)}{gR} = \frac{WS_a(T_n)}{g}\frac{C_\mu \eta}{\mu} \tag{20}$$

where $S_a(T_n)$ is the design spectral acceleration at T_n.

10th step: Calculate the difference between the desired yield base shear of SMRF $V_{\mathrm{SMRF,d}}$ and actual yield base shear $V_{\mathrm{y,SMRF}}$, as well as the difference between C_μ and $C_{\mu,t}$:

$$\frac{\left|V_{\mathrm{SMRF},d} - V_{\mathrm{y,SMRF}}\right|}{V_{\mathrm{y,SMRF}}} \le tol \tag{21}$$

$$\frac{\left|C_{\mu}-C_{\mu,\mathrm{t}}\right|}{C_{\mu,\mathrm{t}}} \le tol \tag{22}$$

The values of η and λ should be changed from the 7th step until the difference is lower than the desired level (*tol*). *tol* is set as 5% in this paper. Note that while $V_{\mathrm{SMRF,d}}$ is larger than $V_{\mathrm{y,SMRF}}$, the values η and λ can be decreased and increased, respectively.

11th step: The values of T, η, λ, α_1, α_2, β, and μ can be determined through the above design steps. The corresponding C_r can be obtained based on the developed ANN model.

12th step: Calculate the target residual displacement ratio $C_{r,t}$ based on the assumption that the residual lateral displacement profile of RSMRF is the same as the maximum lateral displacement profile:

$$C_{r,t} = \frac{\Delta_r}{\Delta_e} \tag{23}$$

$$\Delta_r = \frac{\sum_{i=1}^{n}\left[m_i \Delta_{i,r}{}^2\right]}{\sum_{i=1}^{n} m_i \Delta_{i,r}} \tag{24}$$

$$\Delta_{i,r} = P_1 \theta_{r,t} h_i (1 - P_2 \frac{h_i}{H}) \tag{25}$$

If C_r is larger than $C_{r,t}$, the design process should be continued from the 13th step; otherwise, the design process should be continued from the 16th step.

13th step: Assume new values of η and λ. The fundamental period of RSMRF can be calculated through Eqs. (16) and (17). The relationship between C_r and μ can be obtained based on the developed ANN model. Then the corresponding μ that is related to $C_{r,t}$ can be obtained.

14th step: Based on the new values of T, η, λ, α_1, α_2, β, and μ, the corresponding values of C_μ can be updated through the developed ANN model.

15th step: The desired yield displacement of SMRF $\Delta_{y,d}$ can be estimated as:

$$\Delta_{y,d} = \frac{\Delta_d}{\mu} \tag{26}$$

$$\Delta_d = C_\mu S_d(T_n) \tag{27}$$

The yield inter-story drift ratio of SMRF θ_y can be estimated as:

$$\theta_y = \frac{\Delta_{y,d} \sum_{i=1}^{n} m_i P_1 h_i (1 - P_2 \frac{h_i}{H})}{\sum_{i=1}^{n} m_i \left[P_1 h_i (1 - P_2 \frac{h_i}{H}) \right]^2} \tag{28}$$

The desired yield base shear of SMRF can be calculated as:

$$V_{\mathrm{SMRF},d} = \frac{W S_a(T_n)}{gR} = \frac{W S_a(T_n)}{g} \frac{C_\mu \eta}{\mu} \tag{29}$$

The difference between θ_y and $\theta_{y,\mathrm{SMRF}}$ and that between $V_{\mathrm{SMRF},d}$ and $V_{y,\mathrm{SMRF}}$ can be obtained through Eqs. (30) and (31), respectively. The values of η and λ should be changed from the 14th step until the difference is lower than the desired level (*tol*). Note that while $V_{\mathrm{SMRF,d}}$ is larger than $V_{y,\mathrm{SMRF}}$, the values η and λ can be decreased and increased, respectively.

$$\frac{\left| \theta_y - \theta_{y,\mathrm{SMRF}} \right|}{\theta_{y,\mathrm{SMRF}}} \le tol \tag{30}$$

$$\frac{\left| V_{\mathrm{SMRF},d} - V_{y,\mathrm{SMRF}} \right|}{V_{y,\mathrm{SMRF}}} \le tol \tag{31}$$

16th step: The contribution of self-centering braces on the lateral story stiffness and base shear can be obtained after obtaining the final values of η and λ:

$$K_{\mathrm{S},i} = \frac{1-\eta}{\eta} K_{\mathrm{SMRF},i} \tag{32}$$

$$V_{\mathrm{y,S}} = \lambda V_{\mathrm{y,SMRF}} \tag{33}$$

where $K_{\mathrm{SMRF},i}$ is the lateral stiffness of the i^{th} story of existing SMRF.

The corresponding lateral seismic forces can be calculated through distributing $V_{\mathrm{y,S}}$ with the distribution factor $C_{V,i}$:

$$F_i = C_{V,i} V_{\mathrm{y,S}} \tag{34}$$

$$C_{V,i} = \frac{m_i h_i}{\sum_{j=1}^{n} m_j h_j} \tag{35}$$

The story shear force can be obtained as:

$$V_{\mathrm{y,S},i} = \sum_{i}^{n} F_i \tag{36}$$

If we assume that the self-centering braces are installed in the gravity frame with an inverted V-type configuration (as shown in Fig. 7), the initial axial stiffness and yield strength of the self-centering braces can be calculated as:

$$k_{\mathrm{S},i} = \frac{K_{\mathrm{S},i}}{N \cos^2 \varphi_i} \tag{37}$$

$$F_{\mathrm{S},i} = \frac{V_{\mathrm{y,S},i}}{N \cos \varphi_i} \tag{38}$$

According to the design procedure introduced in [40], the self-centering braces can be designed based on $k_{\mathrm{S},i}$ and $F_{\mathrm{S},i}$. Stiffeners can be installed to strengthen beams and columns if they cannot resist the additional forces introduced by self-centering braces.

17th step: The seismic performance of the designed RSMRF should be evaluated through nonlinear dynamic analysis. If the designed RSMRF cannot achieve the target performance objective, the design can be adjusted by scaling the self-centering brace's capacity or changing $C_{V,i}$.

5. DESIGN CASES

Fig. 7 shows the three- and nine-story SMRF buildings considered in this section to validate the proposed PRDBD method. The three- and nine-story SMRFs are denoted as SMRF3 and SMRF9, respectively. The original SMRF3 and SMRF9 were designed by Brandow & Johnston Associates for the SAC Phase Ⅱ Steel Project [45]. Although these two buildings were not experimentally tested, many past studies have investigated the properties of SMRF3 and SMRF9 numerically [4, 5, 45, 46]. These buildings were designed as office buildings located in Los Angeles. The corresponding site classification is class D. The corresponding design spectrum parameters, including S_{DS}, S_{D1}, and T_L, are set as 1.393 g, 0.77 g, and 8 s, respectively. As shown in Figs. 7(a) and 7(e), the bay width of SMRF3 and SMRF9 is 9.15 m. The elevations of SMRF3 and SMRF9 are shown in Figs. 7(c) and 7(g), respectively. The story height of SMRF3 is 3.96 m. SMRF9 has a basement with a height of 3.65 m. The first story height of SMRF9 is 5.49 m, while the other story height is 3.96 m. The design information of the beams and columns included in SMRF3 and SMRF9 is shown in Figs. 7(c) and 7(g). Figs. 7(b) and 7(d) show the arrangement of the self-centering braces in SMRF3, Figs. 7(f), and 7(h) show the arrangement of the self-centering braces in SMRF9. The self-centering braces are installed in two bays of gravity frames in each direction of SMRF3 and SMRF9. The braced bay with self-centering braces in the retrofitted SMRF3 and SMRF9 are denoted as SCBF3 and SCBF9, respectively. The retrofitted SMRF3 and SMRF9 are denoted as RSMRF3 and

RSMRF9, respectively. Owing to the symmetric arrangement, only a 2-D frame was analyzed in this research.

For demonstration, two different sets of performance objectives were set for RSMRF3 and RSMRF9: (a) $\theta_{\mathrm{m,t}}$ = 2% and $\theta_{\mathrm{r,t}}$ = 0.2% under MCE; and (b) $\theta_{\mathrm{m,t}}$ = 2.5% and $\theta_{\mathrm{r,t}}$ = 0.05% under MCE. Accordingly, the two different RSMRF3 systems designed with performance objectives (a) and (b) are denoted as RSMRF3A and RSMRF3B, respectively; while the two different RSMRF9 systems designed with performance objectives (a) and (b) are denoted as RSMRF9A and RSMRF9B, respectively. The initial parameters of SMRF3 were estimated as $V_{y,\mathrm{SMRF}}$ = 4,269 kN, α_1 = 0.0657, and $\theta_{\mathrm{y,SMRF}}$ = 0.77%, while that of SMRF9 were estimated as $V_{y,\mathrm{SMRF}}$ = 6,329 kN, α_1 = 0.0499, and $\theta_{\mathrm{y,SMRF}}$ = 0.92%. The hysteretic parameters of the self-centering brace were set as α_2 = 0.16 and β = 0.5 for a demonstration. Based on the proposed PRDBD method, the values of η and λ were obtained as 0.35 and 0.52, respectively, for RSMRF3A; 0.41 and 0.46, respectively, for RSMRF3B; 0.39 and 1.95, respectively, for RSMRF9A; and 0.58 and 1.90, respectively, for RSMRF9B. Table 2 shows the design information of the self-centering braces included in RSMRF3A, RSMRF3B, RSMRF9A, and RSMRF9B. In Table 2, D, d, H_0, and $t^{'}$ are the geometries of the disc spring, as illustrated in Fig. 1(b). n_{f} and n_{p} are the set number of the disc spring stacked in series and the number of disc spring stacked in parallel in each set, respectively. The following briefly introduces the design process of RSMRF9A and RSMRF9B from the 6th step.

(1) Design process of RSMRF9A

6th step: Based on the ratio of column's strength to beam's strength of SMRF9, the values of P_1 and P_2 were set as 0.85 and 0.3, respectively. Accordingly, based on Eqs. (10) to (14), the ductility ratio μ is calculated as 2.1739.

7th step: The initial values of η and λ were set as 0.5 and 0.5, respectively. Note that the initial values of η *and* λ can be chosen arbitrarily for the initial design. The natural frequency of the existing SMRF9 $\omega_{\mathrm{n,SMRF}}$ was obtained as 2.9451 Hz based on the eigenvalue analysis that will be introduced in Section 6. Based on Eqs. (16) and (17), the fundamental period of RSMRF9 T_n was estimated as 1.5086 s. The corresponding C_μ was obtained based on the developed ANN model as 0.8655.

8th step: Based on Eqs. (18) and (19), the target inelastic displacement ratio $C_{\mu,t}$ was calculated as 0.7703.

9th step: Based on Eq. (20), the desired yield base shear of SMRF was calculated as 6861.1 kN.

10th step: Based on Eqs. (21) and (22), the difference between the desired yield base shear of SMRF $V_{\mathrm{SMRF,d}}$ and actual yield base shear $V_{\mathrm{y,SMRF}}$ as well as the difference between C_μ and $C_{\mu,t}$ were calculated as 8.41% and 12.36%, respectively, that are larger than 5%. After six iterative calculations, the values of η and λ were obtained as 0.39 and 1.95, respectively. The corresponding difference between $V_{\mathrm{SMRF,d}}$ and $V_{\mathrm{y,SMRF,}}$ as well as the difference between C_μ and $C_{\mu,t}$, were calculated as 3.72% and 0.21%, respectively, which are smaller than 5%. The corresponding fundamental period was 1.3323 s.

11th step: The values of T, η, λ, α_1, α_2, β, and μ were obtained as 1.3323 s, 0.39, 1.95, 0.0499, 0.16, 0.5, and 0.8704, respectively. Based on the developed ANN model, the corresponding C_r can be obtained as 0.0181.

12th step: Based on Eqs. (23) to (25), the target residual displacement ratio $C_{r,t}$ was obtained as 0.0872 that is larger than C_r (i.e., 0.0181), indicating that when the maximum inter-story drift of RSMRF9 is lower than 2%, the corresponding residual inter-story drift is lower than 0.2%. Then, the design step can continue from the 16th step.

16th step: Based on Eqs. (32) to (38), the initial stiffness and strength of self-centering braces can be calculated. Table 2 shows the design information of the self-centering braces included in RSMRF9A.

(2) Design process of RSMRF9B

6th step: Based on Eqs. (10) to (14), the ductility ratio μ is calculated as 2.7174.

7th step: The initial values of η and λ were set as 0.5 and 0.5, respectively. The natural frequency of the existing SMRF9 $\omega_{\mathrm{n,SMRF}}$ was obtained as 2.9451 based on engine analysis that will be introduced in Section 6. Based on Eqs. (16) and (17), the fundamental period of RSMRF9 T_n was estimated as 1.5086 s. The corresponding C_μ was obtained based on the developed ANN model as 0.8372.

8th step: Based on Eqs. (18) and (19), the target inelastic displacement ratio $C_{\mu,t}$ was calculated as 0.9629.

9th step: Based on Eq. (20), the desired yield base shear of SMRF was calculated as 5309.4 kN.

10th step: Based on Eqs. (21) and (22), the difference between $V_{\mathrm{SMRF,d}}$ and $V_{\mathrm{y,SMRF,}}$ as well as the difference between C_μ and $C_{\mu,t}$, were calculated as 16.11% and 13.05%, respectively, which are larger than 5%. The iterative calculation was conducted by changing the values of η and λ to satisfy the error requirement. Finally, the values of η and λ were obtained as 0.68 and 1.75, respectively. The corresponding difference between $V_{\mathrm{SMRF,d}}$ and $V_{\mathrm{y,SMRF}}$ as well as the difference between C_μ and $C_{\mu,t}$ were calculated as 3.22% and 0.31%, respectively, which are smaller than 5%.

11th step: The values of T, η, λ, α_1, α_2, β, and μ were obtained as 1.7593 s, 0.68, 1.75, 0.0499, 0.16, 0.5, and 0.8283, respectively. Based on the developed ANN model, the corresponding C_r can be obtained as 0.0203.

12th step: Based on Eqs. (23) to (25), the target residual displacement ratio $C_{r,t}$ was obtained as 0.0165 that is smaller than C_r (i.e., 0.0203), indicating that when the maximum inter-story drift of RSMRF9 is lower than 2.5%, the corresponding residual inter-story drift is still much larger than 0.05%. Then, the design step can continue from the 13th step.

13th step: The values of η and λ obtained in the 10th step (i.e., 0.68 and 1.75, respectively) were used in this step. The corresponding μ that is related to $C_{r,t}$ can be obtained as 3.3601.

14th step: The values of T, η, λ, α_1, α_2, β, and μ were obtained as 1.7593 s, 0.68, 1.75, 0.0499, 0.16, 0.5, and 3.3601, respectively. The corresponding values of C_μ can be obtained through the developed ANN model as 0.8002.

15th step: The desired yield inter-story drift ratio of SMRF θ_{y} can be estimated based on Eqs. (26) to (28) as 0.72%. The desired yield base shear of SMRF can be calculated based on Eq. (29) as 4786.1 kN. The difference between θ_{y} and $\theta_{\mathrm{y,SMRF}}$ and that between $V_{\mathrm{SMRF},d}$ and $V_{\mathrm{y,SMRF}}$ can be obtained through Eqs. (30) and (31) as 21.62% and 24.38%, respectively, which are much larger than 5%. The iterative calculation was conducted by changing the values of η and λ to satisfy the error requirement. Finally, the values of η and λ were obtained as 0.58 and 1.9, respectively. The difference between θ_{y} and $\theta_{\mathrm{y,SMRF}}$ and that between $V_{\mathrm{SMRF},d}$ and $V_{\mathrm{y,SMRF}}$ can be obtained through Eqs. (30) and (31) as 3.24% and 3.9%, respectively, which are much smaller than 5%. The corresponding fundamental period was 1.6248 s.

16th step: Based on Eqs. (32) to (38), the initial stiffness and strength of self-centering braces can be calculated. Table 2 shows the design information of the self-centering braces included in RSMRF9B.

Based on the presented design processes of RSMRF9A and RSMRF9B, it can be found that the design of RSMRF9A is governed by the maximum inter-story drift, wherein the residual inter-story drift is lower than the target value when the RSMRF9A achieves the target maximum inter-story drift; and the design of RSMRF9B is governed by the residual inter-story drift, wherein the maximum inter-story drift is lower than the target value when the RSMRF9A achieves the target residual inter-story drift.

6. Performance evaluation

6.1. Numerical modeling

OpenSees [47] was used to develop the numerical models of the considered systems and perform the nonlinear static and dynamic analyses. Fig. 8(a) sketches the numerical model of RSMRF9A. The beam-to-column connections in SCBF9 and the exterior beam-to-column connections on the right side of SMRF9 were modeled as pinned connections. Assume sufficient stiffeners were installed in the beams and columns of the gravity frame to resist the additional forces introduced by self-centering braces and ensure the beams and columns of the gravity frame maintain elastic during earthquakes. For simplicity, *Elastic Beam-Column* elements were used to model the beams and columns of the gravity frame. The hysteretic behavior of the self-centering braces was simulated using *Two-Node-Link* elements with the *SelfCentering* material model. Fig. 8(b) compares the test results of the considered self-centering brace in [40] and the numerical results obtained through the proposed modeling method. As shown, the numerical results agree well with the test results, confirming the accuracy of the proposed modeling method for the self-centering brace. The modified Ibarra-Medina-Krawinkler model [48, 49] was adopted to model the hysteretic behavior of the beam-to-column connections in SMRF9 in consideration of strength deterioration. The panel zone’s deformation was considered based on the investigation of Gupta [50]. The detailed modeling information of the beam-to-column connections included in SMRF9 can be found in Fig. 8(a). The *Force-Based Beam-Column* elements were used to model the beams and columns included in SMRF9. *Equal*

DOF commends were used to make SCBF9 and RSMRF9 achieve the same horizontal and vertical displacement at each story. The P-Δ effects were considered through the leaning column connected to the adjacent column of SMRF9 through rigid truss elements. The numerical models of SMRF3, RSMRF3A, RSMRF3B, SMRF9, and RSMRF9B were also developed by following the same methodology.

The modal properties of the designed frames were investigated through eigenvalue analyses. The fundamental periods of SMRF3, RSMRF3A, RSMRF3B, are 0.919 s, 0.527 s, and 0.564 s, respectively; those of SMRF9, RSMRF9A, and RSMRF9B are 2.133 s, 1.359 s, and 1.556 s, respectively. It can be found that the fundamental periods of RSMRF9A and RSMRF9B obtained from the numerical analysis were close to the estimated values in Section 5 (i.e., 1.3323 s and 1.6248 s for RSMRF9A and RSMRF9B, respectively). Moreover, the fundamental periods of SMRF3 and SMRF9 are close to those obtained in Ohtori et al. [45] (i.e., 1.010 s and 2.257 s, respectively), confirming the accuracy of the developed numerical models of SMRF3 and SMRF9.

6.2. Nonlinear static analysis

Pushover analyses were conducted to investigate the static nonlinear behavior of SMRF3, RSMRF3A, RSMRF3B, SMRF9, RSMRF9A, and RSMRF9B. The monotonous pushover curves are shown in Fig. 9. The pushover analysis ended at the roof drift of 5%. The base shear of the considered systems was normalized by building weight. As shown in Fig. 9, the installation of self-centering braces can efficiently increase the stiffness and strength of SMRF3 and SMRF9. Because of the damage of beam-to-column connections, SMRF3 and SMRF9 show obvious strength deterioration at about 3.2% and 2.5% roof drifts, respectively. However, no strength deterioration can be found in RSMRF3A, RSMRF3B, RSMRF9A, and RSMRF9B when the roof drift is loaded up to 5%. These observations confirm that the self-centering braces can effectively improve the seismic performance of the existing SMRF9.

6.3. Nonlinear dynamic analysis

20 ground motions were selected from the NGA Database [51] and scaled to make the median acceleration spectrum of the selected ground motions capture the MCE design spectrum defined in ASCE 7-16 [52] for the dynamic analyses under MCE. Note that the 20 ground motions are chosen intentionally different from the ground motion sets used in Section 2, aiming to evaluate the efficacy of the developed C_μ and C_r prediction models and the proposed design procedure when different ground motions are used. Table 3 shows the detailed information and scale factors of the selected ground motions. The comparison between the design spectrum and the spectral accelerations of the selected ground motion is shown in Fig. 10. The selected ground motions can match well with the MCE design spectrum. To obtain the residual inter-story drift responses of the considered frames, 20 s free vibration was added to the end of each dynamic analysis.

Fig. 11 shows the peak inter-story drifts of the considered systems under the selected ground motions with the MCE intensity. The designed frames show variable responses under different ground motion excitations. The inter-story drift concentration mechanism can be observed in the considered systems. Improving the inter-story drift distribution of steel moment-resisting frames is beyond the scope of the present paper. The related research work can be found in [4, 53]. This paper is focused on mitigating the peak and residual inter-story drift responses of the existing steel moment-resisting frames to the desired level by installing self-centering braces. The maximum median peak inter-story drifts of SMRF3 and SMRF9 are 3.44% and 2.93%, respectively, whereas those of RSMRF3A, RSMRF3B, RSMRF9A, and

RSMRF9B are only 1.92%, 2.27%, 1.99%, and 2.02%, respectively, indicating that self-centering braces can efficiently reduce the peak inter-story drift responses of the original SMRF3 and SMRF9. Fig. 12 shows the residual inter-story drifts of the considered systems under MCE. The maximum median residual inter-story drifts of SMRF3 and SMRF9 are 0.64% and 0.86%, respectively, whereas those of RSMRF3A, RSMRF3B, RSMRF9A, and RSMRF9B are 0.038%, 0.047%, 0.043%, and 0.055%, respectively, indicating that self-centering braces can efficiently reduce the residual inter-story drift responses of the original SMRF3 and SMRF9. The RSMRF3A and RSMRF9A show better performance than RSMRF3B and RSMRF9B in controlling residual inter-story drifts. The reason for this phenomenon is that self-centering braces included in RSMRF3A and RSMRF9A have higher stiffness and strength than that included in RSMRF3B and RSMRF9B, making the RSMRF3A and RSMRF9A achieve better self-centering capacities. According to FEMA P-58 [54], no structural realignment is necessary after earthquakes when the residual inter-story drift (θ_r) is lower than 0.2%, the structural members can be repaired with low economic loss when θ_r is lower than 0.5%, and the structural members can be repaired with great economic loss when θ_r is larger than 0.5% and lower than 1.0%. Based on the investigation by McCormick et al. [3], it is a better and more economic choice to demolish and rebuild rather than repair the buildings with θ_r larger than 0.5%. Accordingly, the SMRF3 and SMRF9 will be demolished due to great repair costs, whereas RSMRF3A, RSMRF3B, RSMRF9A, and RSMRF9B can continue to provide service without repair requirements after earthquakes with MCE intensity. By following the design process presented in Section 5, the designs of RSMRF3A and RSMRF9A are governed by the maximum inter-story drift; consequently, the maximum median peak inter-story drifts of RSMRF3A and RSMRF9A are close to the target (i.e., 2.0%), whereas the maximum median residual inter-story drifts of RSMRF3A and

RSMRF9A are much lower than the target (i.e., 0.2%). In contrast, the designs of RSMRF3B and RSMRF9B are governed by the residual inter-story drift; the maximum median peak inter-story drifts of RSMRF3B and RSMRF9B are much lower than the target (i.e., 2.5%), whereas the maximum median residual inter-story drifts of RSMRF3B and RSMRF9B are close to the target (i.e., 0.05%). These phenomena confirm that the RSMRFs designed through the proposed PRDBD method can achieve the desired performance objectives that are defined by the maximum and residual inter-story drifts.

7. CONCLUSIONS

This paper developed a peak and residual displacement-based design (PRDBD) method for controlling the peak and residual inter-story drift responses of SMRF by installing self-centering braces. The three- and nine-story SMRFs were upgraded using the proposed PRDBD method to meet two different sets of performance objectives. Static and dynamic analyses were conducted to investigate the seismic performance of the designed buildings. Based on the analysis results, the following conclusions can be obtained:

- The developed ANN models can accurately predict the median values of C_μ and C_r of RSMRF with R^2 values of 0.9936 and 0.9512, respectively. A software named ANNRSMRF-MEDIAN was developed and provided to facilitate the prediction of C_μ and C_r with the inputs of T, η, λ, α_1, α_2, β, and μ.
- SMRF3 and SMRF9 show obvious deterioration of strength at about 3.2% and 2.5% roof drifts, respectively; whereas no strength deterioration can be found in RSMRF3A, RSMRF3B, RSMRF9A, and RSMRF9B when the roof drift is loaded up to 5%, confirming the efficiency of self-centering braces in enhancing the lateral force-resisting capacity of the existing SMRFs.

- The maximum inter-story drifts of RSMRF3A and RSMRF9A are close to 2.0% while the residual inter-story drifts are lower than 0.2%, and the residual inter-story drifts of RSMRF3B and RSMRF9B are close to 0.05% while the maximum inter-story drifts are lower than 2.5% under MCE. These results confirm that the proposed PRDBD method can efficiently make the designed RSMRFs achieve the desired maximum and residual inter-story drift responses under the concerned seismic intensity.
- The SMRF3 and SMRF9 will be demolished because the residual inter-story drift is larger than 0.5%, whereas RSMRF3A, RSMRF3B, RSMRF9A, and RSMRF9B can continue to provide service without repair requirements after MCE earthquakes by achieving residual inter-story drifts lower than 0.2%.

It is noteworthy that although the modeling methods of SMRF and self-centering braces have been verified separately through the past investigations or test results, further tests of RSMRF need to be conducted in the future to investigate the seismic performance of RSMRF and the efficacy of the proposed design method before the RSMRF is used in practical applications.

ACKNOWLEDGMENT

The financial support from the Research Grants Council of Hong Kong (Grant Nos. PolyU 152246/18E, C7038-20G, T22-502/18-R), and the Hong Kong Polytechnic University (Grant Nos. ZE2L, ZVX6, and P0038795).

APPENDIX A. SUPPLEMENTARY DATA

The software installer of ANNRSMRF-MEDIAN.

REFERENCES

[1] Cole GL, Dhakal RP, Turner FM. Building pounding damage observed in the 2011 Christchurch earthquake. Earthquake Engineering & Structural Dynamics. 2012;41:893-913.

[2] Howes T, Cheesebrough T. Infrastructure impact and recovery following the 2010–2011 earthquakes in Christchurch, New Zealand. Proceedings of the Institution of Civil Engineers-Civil Engineering: Thomas Telford Ltd; 2013. p. 57-64.

[3] McCormick J, Aburano H, Ikenaga M, Nakashima M. Permissible residual deformation levels for building structures considering both safety and human elements. Proceedings of the 14th world conference on earthquake engineering2008. p. 12-7.

[4] Hu S, Wang W, Alam MS. Performance-based seismic design method for retrofitting steel moment-resisting frames with self-centering energy-absorbing dual rocking core system. Journal of Constructional Steel Research. 2022;188:106986.

[5] Hu S, Wang W, Qu B. Seismic economic losses in mid-rise steel buildings with conventional and emerging lateral force resisting systems. Engineering Structures. 2020;204:110021.

[6] Achour N, Miyajima M, Kitaura M, Price A. Earthquake-induced structural and nonstructural damage in hospitals. Earthquake spectra. 2011;27:617-34.

[7] Miranda E, Mosqueda G, Retamales R, Pekcan G. Performance of nonstructural components during the 27 February 2010 Chile earthquake. Earthquake Spectra. 2012;28:453-71.

[8] Hu S, Wang W, Alam MS. Hybrid self-centering rocking core system with fiction spring and viscous dampers for seismic resilience. Engineering Structures. 2022;257:114102.

[9] Hu S, Zhu S, Wang W. Hybrid self-centering companion spines for structural and nonstructural damage control. Engineering Structures. 2022;266:114603.

[10] Priestley MN, Sritharan S, Conley JR, Pampanin S. Preliminary results and conclusions from the PRESSS five-story precast concrete test building. PCI journal. 1999;44:42-67.

[11] Ricles JM, Sause R, Garlock MM, Zhao C. Posttensioned seismic-resistant connections for steel frames. Journal of Structural Engineering. 2001;127:113-21.

[12] Garlock MM, Ricles JM, Sause R. Experimental studies of full-scale posttensioned steel connections. Journal of Structural Engineering. 2005;131:438-48.

[13] Garlock MM, Ricles JM, Sause R. Influence of design parameters on seismic response of post-tensioned steel MRF systems. Engineering Structures. 2008;30:1037-47.

[14] Chou C-C, Chen J-H. Development of floor slab for steel post-tensioned self-centering moment frames. Journal of Constructional Steel Research. 2011;67:1621-35.

[15] Zhang Y, Xu L. Cyclic response of a self-centering RC wall with tension-compression-coupled disc spring devices. Engineering Structures. 2022;250:113404.

[16] Liu J, Xu L, Li Z. Development and experimental validation of a steel plate shear wall with self-centering energy dissipation braces. Thin-Walled Structures. 2020;148:106598.

[17] Xu L, Xiao S, Li Z. Experimental investigation on the seismic behavior of a new self-centering shear wall with additional friction. Journal of Structural Engineering. 2021;147:04021056.

[18] Eatherton MR, Ma X, Krawinkler H, Deierlein GG, Hajjar JF. Quasi-static cyclic behavior of controlled rocking steel frames. Journal of Structural Engineering. 2014;140:04014083.

[19] Eatherton MR, Ma X, Krawinkler H, Mar D, Billington S, Hajjar JF et al. Design concepts for controlled rocking of self-centering steel-braced frames. Journal of Structural Engineering. 2014;140:04014082.

[20] Hu S, Wang W, Qu B. Seismic evaluation of low-rise steel building frames with self-centering energy-absorbing rigid cores designed using a force-based approach. Engineering Structures. 2020;204:110038.

[21] Hu S, Wang W, Qu B. Self-centering companion spines with friction spring dampers: Validation test and direct displacement-based design. Engineering Structures. 2021;238:112191.

[22] Hu S, Wang W, Qu B, Alam MS. Development and validation test of a novel Self-centering Energy-absorbing Dual Rocking Core (SEDRC) system for seismic resilience. Engineering Structures. 2020;211:110424.

[23] Hu S, Wang W, Qu B, Alam MS. Self-centering energy-absorbing rocking core system with friction spring damper: Experiments, modeling and design. Engineering Structures (under review). 2020.

[24] Zhang G, Xu L-H, Li Z-X. Development and seismic retrofit of an innovative modular steel structure connection using symmetrical self-centering haunch braces. Engineering Structures. 2021;229:111671.

[25] Xu L, Chen P, Li Z. Development and validation of a versatile hysteretic model for pre-compressed self-centering buckling-restrained brace. Journal of Constructional Steel Research. 2021;177:106473.

[26] Xu L, Lin Z, Xie X. Assembled self-centering energy dissipation braces and a force method-based model. Journal of Constructional Steel Research. 2022;190:107121.

[27] Xu LH, Fan XW, Li ZX. Cyclic behavior and failure mechanism of self‐centering energy dissipation braces with pre‐pressed combination disc springs. Earthquake Engineering & Structural Dynamics. 2017;46:1065-80.

[28] Wang W, Fang C, Zhao Y, Sause R, Hu S, Ricles J. Self‐centering friction spring dampers for seismic resilience. Earthquake Engineering and Structural Dynamics. 2019;48:1045-65.

[29] Zhu S, Zhang Y. Seismic analysis of concentrically braced frame systems with self-centering friction damping braces. Journal of Structural Engineering. 2008;134:121-31.

[30] Chou C-C, Chung P-T. Development of cross-anchored dual-core self-centering braces for seismic resistance. Journal of Constructional Steel Research. 2014;101:19-32.

[31] Chou C-C, Hsiao C-H, Chen Z-B, Chung P-T, Pham D-H. Seismic loading tests of full-scale two-story steel building frames with self-centering braces and buckling-restrained braces. Thin-Walled Structures. 2019;140:168-81.

[32] Zhu R, Guo T, Mwangilwa F, Han D. Seismic design of self-centering viscous-hysteretic devices used for steel moment-resisting frames. Engineering Structures. 2021;239:112369.

[33] Shi F, Ozbulut OE, Zhou Y. Influence of shape memory alloy brace design parameters on seismic performance of self‐centering steel frame buildings. Structural Control and Health Monitoring. 2020;27:e2462.

[34] Ozbulut OE, Michael RJ, Silwal B. Seismic Performance Assessment of Steel Frames Upgraded with Self-Centering Viscous Dampers. Dynamics of Civil Structures, Volume 2: Springer; 2015. p. 421-32.

[35] Qiu C, Zhao X, Zhu S. Seismic upgrading of multistory steel moment‐resisting frames by installing shape memory alloy braces: Design method and performance evaluation. Structural Control and Health Monitoring. 2020;27:e2596.

[36] Fang C, Ping Y, Chen Y, Yam M, Chen J, Wang W. Seismic Performance of Self-centering Steel Frames with SMA-viscoelastic Hybrid Braces. Journal of Earthquake Engineering. 2020:1-28.

[37] Longhe, Xu, Xiaowei, Fan, Zhongxian, Li. Experimental behavior and analysis of self-centering steel brace with pre-pressed disc springs - ScienceDirect. Journal of Constructional Steel Research.139:363-73.
[38] Qiu C, Zhu S. Shake table test and numerical study of self‐centering steel frame with SMA braces. Earthquake Engineering & Structural Dynamics. 2017;46:117-37.
[39] Tremblay R, Lacerte M, Christopoulos C. Seismic response of multistory buildings with self-centering energy dissipative steel braces. Journal of structural engineering. 2008;134:108-20.
[40] Wang W, Fang C, Shen D, Zhang R, Ding J, Wu H. Performance assessment of disc spring-based self-centering braces for seismic hazard mitigation. Engineering Structures. 2021;242:112527.
[41] FEMA. FEMA P695. Quantification of building seismic performance factors. Washington, DC: Federal Emergency Management Agency; 2009.
[42] Hu S, Wang W, Alam MS. Probabilistic Nonlinear Displacement Ratio Prediction of Self-centering Energy-absorbing Dual Rocking Core System under Near-fault Ground Motions Using Machine Learning. Journal of Earthquake Engineering. 2021:1-32.
[43] Friedman J, Hastie T, Tibshirani R. The elements of statistical learning: Springer series in statistics New York; 2001.
[44] Karavasilis T, Bazeos N, Beskos D. Maximum displacement profiles for the performance based seismic design of plane steel moment resisting frames. Engineering Structures. 2006;28:9-22.
[45] Ohtori Y, Christenson R, Spencer B, Dyke S. Benchmark control problems for seismically excited nonlinear buildings. Journal of engineering mechanics. 2004;130:366-85.
[46] Fang C, Zhong Q, Wang W, Hu S, Qiu C. Peak and residual responses of steel moment-resisting and braced frames under pulse-like near-fault earthquakes. Engineering Structures. 2018;177:579-97.
[47] Mazzoni S, McKenna F, Scott MH, Fenves GL. OpenSees command language manual. Pacific Earthquake Engineering Research (PEER) Center.2006.
[48] Lignos DG, Krawinkler H. A database in support of modeling of component deterioration for collapse prediction of steel frame structures. Structural Engineering Research Frontiers2007. p. 1-12.
[49] Lignos DG, Krawinkler H. Deterioration modeling of steel components in support of collapse prediction of steel moment frames under earthquake loading. Journal of Structural Engineering. 2011;137:1291-302.
[50] Gupta A. Seismic demands for performance evaluation of steel moment resisting frame structures: Stanford University; 1999.
[51] Chiou B, Darragh R, Gregor N, Silva W. NGA project strong-motion database. Earthquake Spectra. 2008;24:23-44.
[52] ASCE. ASCE/SEI 7-16. Minimum design loads for buildings and other structures. Reston VA: American Society of Civil Engineers; 2016.
[53] Qu B, Sanchez JC, Hou H, Pollino M. Improving inter-story drift distribution of steel moment resisting frames through stiff rocking cores. International Journal of Steel Structures. 2016;16:547-57.
[54] FEMA. FEMA P58. Seismic performance assessment of buildings. Federal Emergency Management Agency; 2012.

Table 1. Values of P_1 and P_2.

Story		1	3	6	9	12	15	18	20
	a_{cd} = 1.1				0.75	0.70	0.65	0.60	0.55
P_1	a_{cd} = 1.3	1	1	0.90	0.80	0.75	0.70	0.65	0.60
	a_{cd} = 1.5				0.85	0.80	0.75	0.70	0.65
P_2		0	0.1	0.2	0.3	0.35	0.4	0.4	0.4

Table 2. Design information of self-centering braces.

System	Story	Yield strength (kN)	Initial stiffness (kN/mm)	D (mm)	d (mm)	H_0 (mm)	t' (mm)	Stack pattern $n_f \times n_p$	Preload of disc spring (kN)	Friction force of the friction plates (kN)
RSMRF3A	1	1451	259	400	200	40	25.1	10 × 4	1088	363
	2	1219	248	400	200	40	24.9	10 × 4	914	305
	3	756	154	400	200	35	23.0	14 × 4	567	189
RSMRF3B	1	1284	200	400	200	40	23.7	10 × 4	963	321
	2	1079	192	400	200	40	23.5	10 × 4	809	270
	3	669	120	400	200	35	21.0	12 × 4	502	167
RSMRF9A	1	9342	300	450	230	50	27.9	8 × 4	7007	2336
	2	7683	499	450	280	50	30.1	8 × 4	5762	1921
	3	7300	428	450	280	50	29.1	8 × 4	5475	1825
	4	6756	414	450	280	50	28.8	8 × 4	5067	1689
	5	6052	378	450	280	50	28.2	8 × 4	4539	1513
	6	5187	361	450	280	50	28.0	8 × 4	3890	1297
	7	4162	247	400	200	40	24.9	10 × 4	3122	1041
	8	2976	205	400	200	40	23.8	10 × 4	2232	744
	9	1630	163	400	200	35	23.4	14 × 4	1223	408
RMRF9B	1	9103	139	400	200	35	21.8	12 × 4	6827	2276
	2	7486	231	400	200	40	24.5	10 × 4	5615	1872
	3	7112	198	400	200	40	23.6	10 × 4	5334	1778
	4	6583	192	400	200	40	23.5	10 × 4	4937	1646
	5	5897	175	400	200	40	23.0	10 × 4	4423	1474
	6	5054	167	400	200	40	21.9	8 × 4	3791	1264
	7	4055	114	400	200	35	20.8	12 × 4	3041	1014
	8	2900	95	400	200	35	19.4	10 × 4	2175	725
	9	1588	75	400	200	35	18.5	10 × 4	1191	397

Table 3. Information of selected ground motions.

No.	Earthquake			Recording Station	Site Data		Scale factor
	M	Year	Name		NEHRP Class	V_{s30} (m/s)	
1	6.5	1942	Borrego	El Centro Array #9	D	213.44	15.8729
2	7.36	1952	Kern County	LA - Hollywood Stor FF	D	316.46	13.1558
3	6.8	1956	El Alamo	El Centro Array #9	D	213.44	18.2496
4	6.61	1971	San Fernando	2516 Via Tejon PV	D	280.56	26.4831
5	6.61	1971	San Fernando	LB - Terminal Island	D	217.92	23.7531
6	6.5	1976	Friuli_ Italy-01	Conegliano	D	352.05	22.436
7	7.35	1978	Tabas_ Iran	Sedeh	D	354.37	37.6477
8	6.53	1979	Imperial Valley-06	Coachella Canal #4	D	336.49	9.608
9	6.36	1983	Coalinga-01	Parkfield - Cholame 12W	D	359.03	17.7385
10	6.5	1983	Taiwan SMART1(25)	SMART1 I01	D	275.82	26.5972
11	6.19	1984	Morgan Hill	APEEL 1E - Hayward	D	219.8	27.5365
12	6.06	1986	N. Palm Springs	Colton Interchange - Vault	D	274.98	23.7887
13	7.3	1986	Taiwan SMART1(45)	SMART1 C00	D	309.41	4.6886
14	7.3	1986	Taiwan SMART1(45)	SMART1 I01	D	275.82	4.372
15	7.3	1986	Taiwan SMART1(45)	SMART1 O01	D	267.67	5.3778
16	7.3	1986	Taiwan SMART1(45)	SMART1 O02	D	285.09	5.267
17	7.3	1986	Taiwan SMART1(45)	SMART1 O08	D	357.43	5.1407
18	6.93	1989	Loma Prieta	Bear Valley #12_ Williams Ranch	D	331.21	4.9069
19	6.93	1989	Loma Prieta	Dublin - Fire Station	D	318.31	9.4326
20	6.93	1989	Loma Prieta	Oakland - Outer Harbor Wharf	D	248.62	2.8088

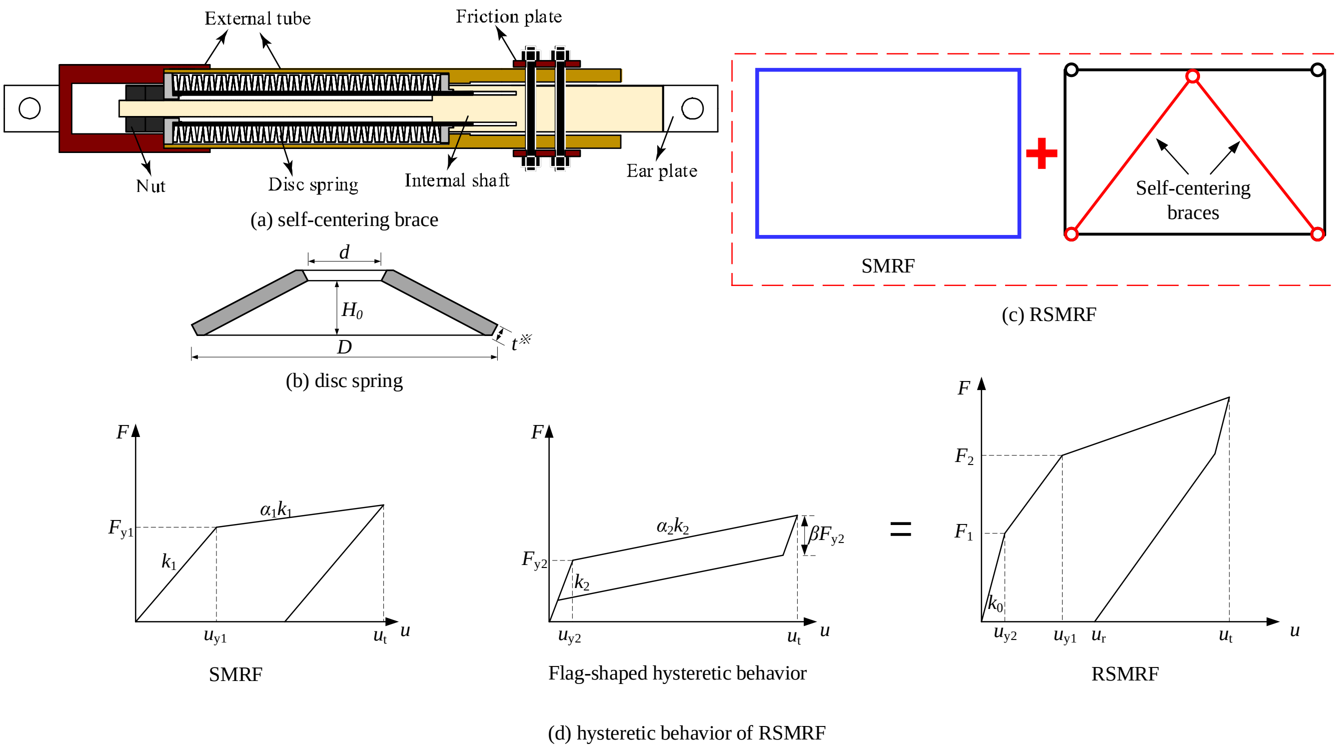

Fig. 1. Illustration of RSMRF.

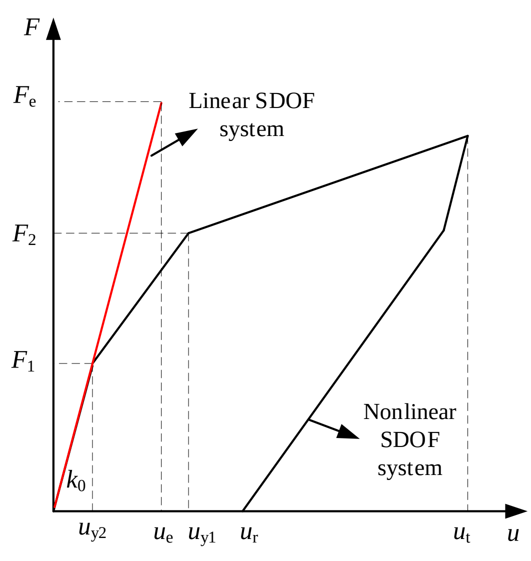

Fig. 2. Illustration of the SDOF systems.

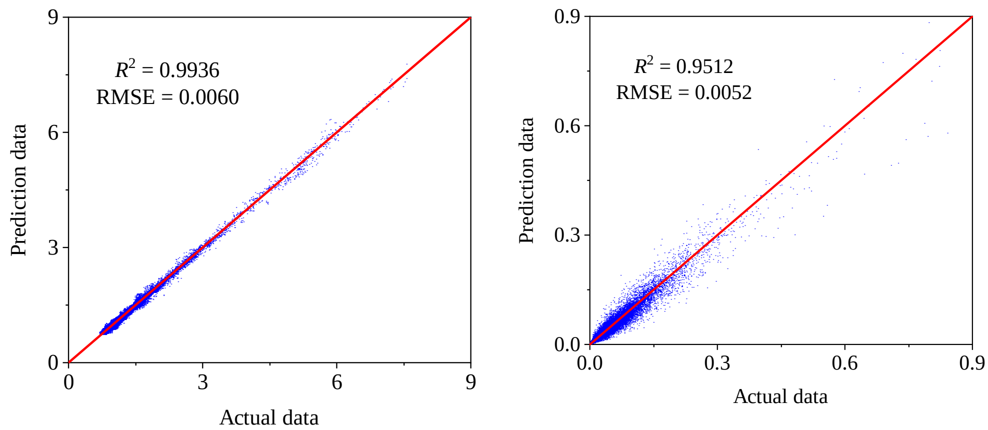

(a) C_μ (b) C_r

Fig. 3. Performance of ANN model.

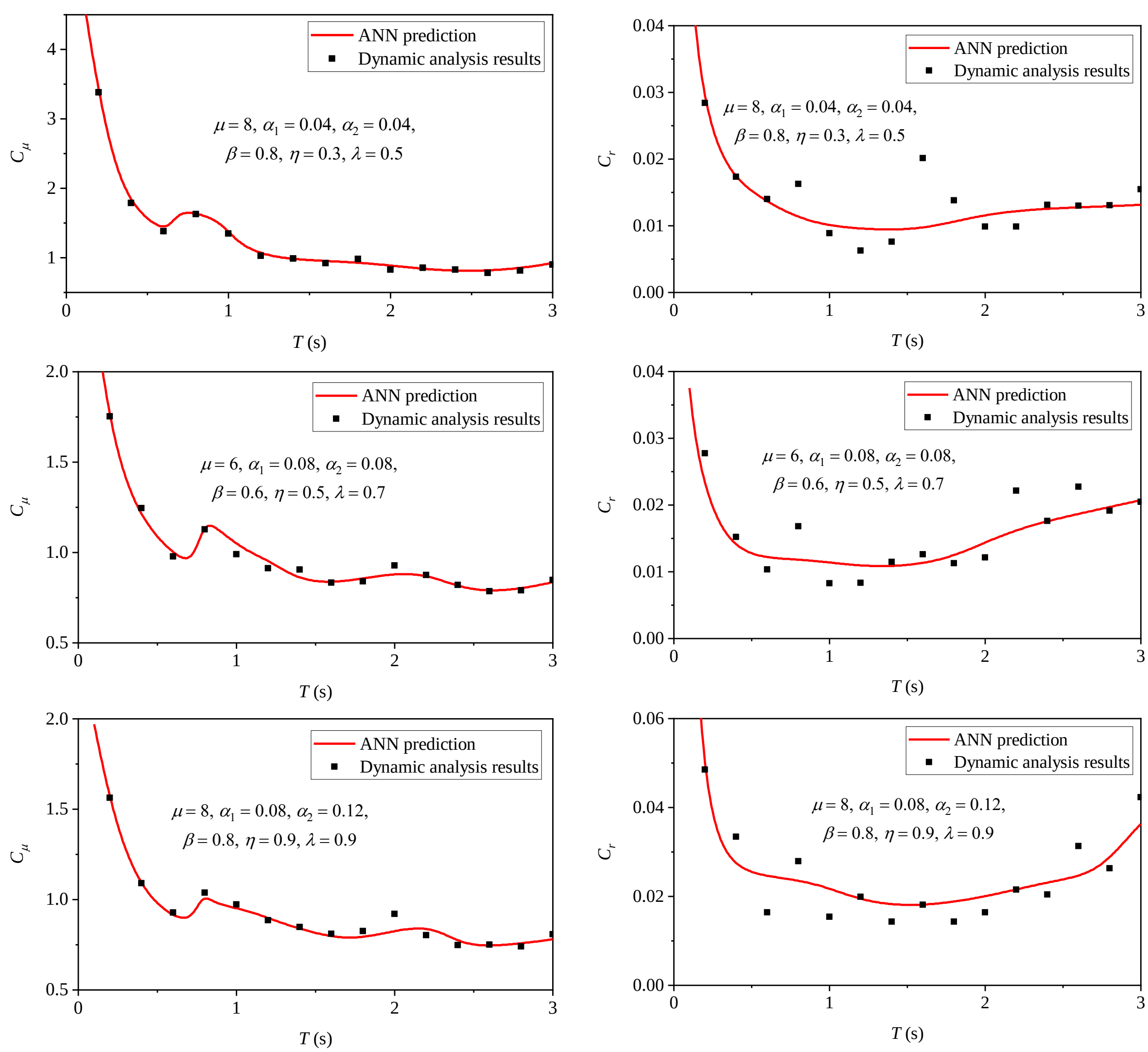

(a) C_μ (b) C_r

Fig. 4. Comparison between ANN prediction and dynamic analysis results of C_μ and C_r.

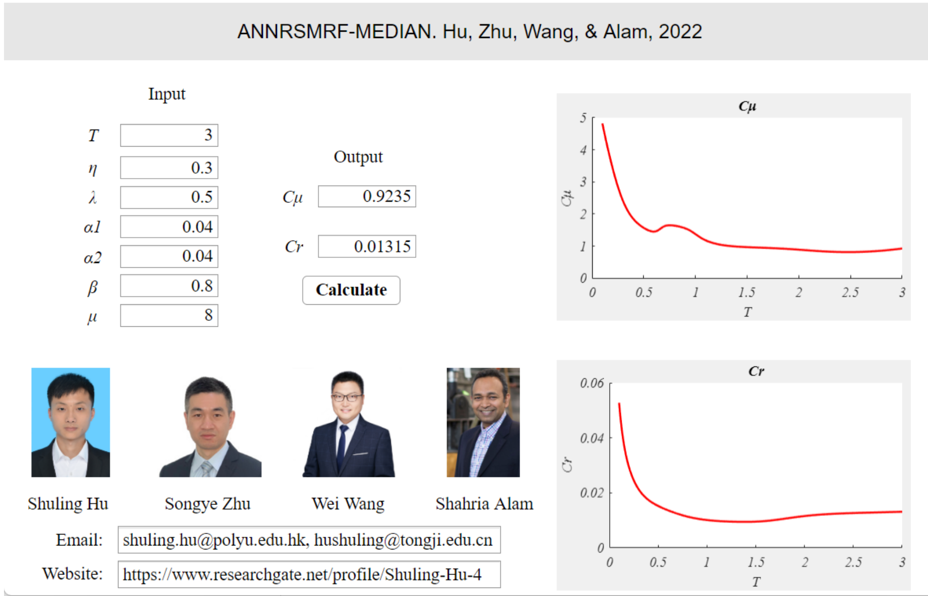

Fig. 5. User interface of ANNRSMRF-MEDIAN.

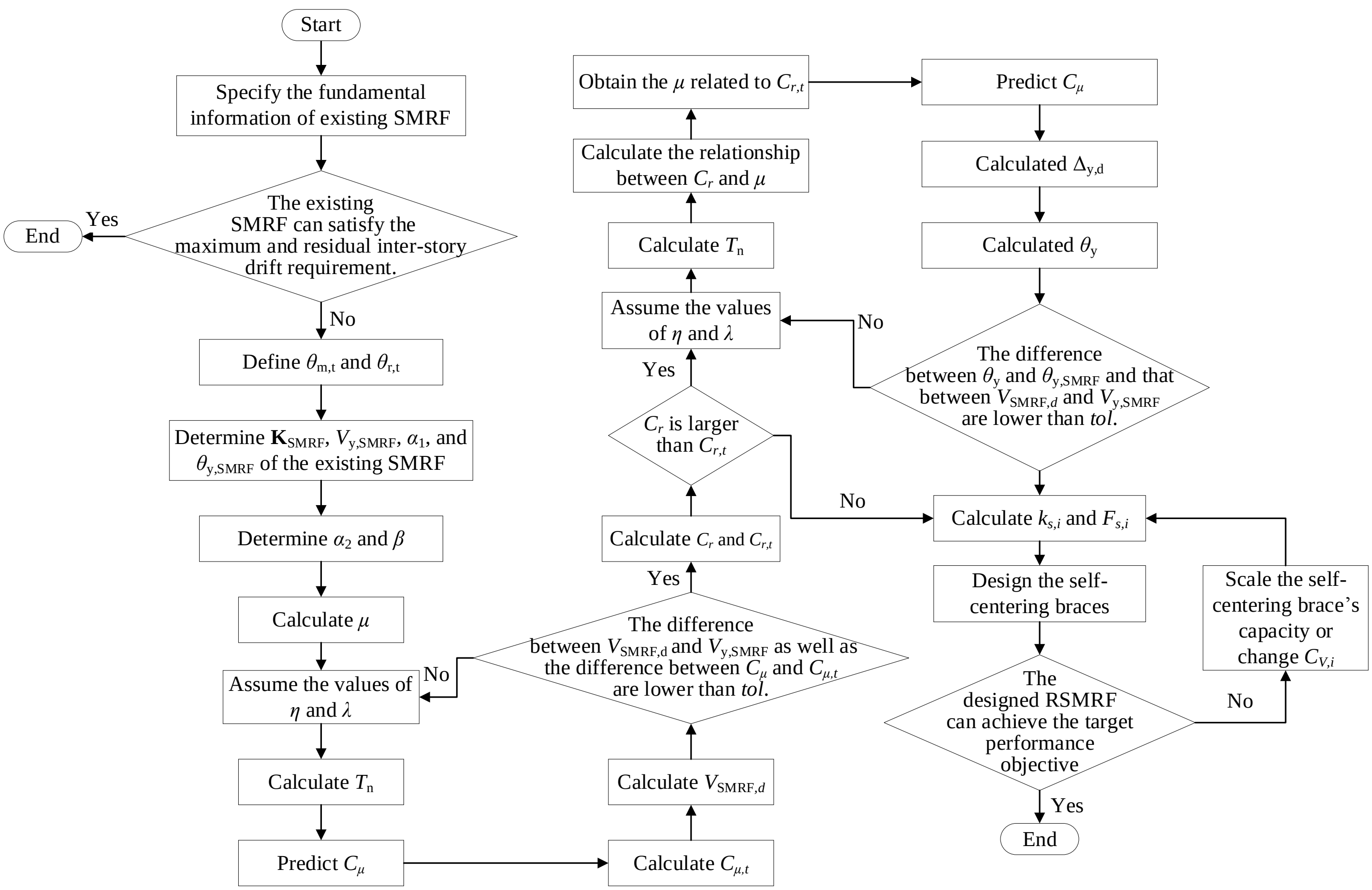

Fig. 6. Flowchart of the proposed PRDBD method.

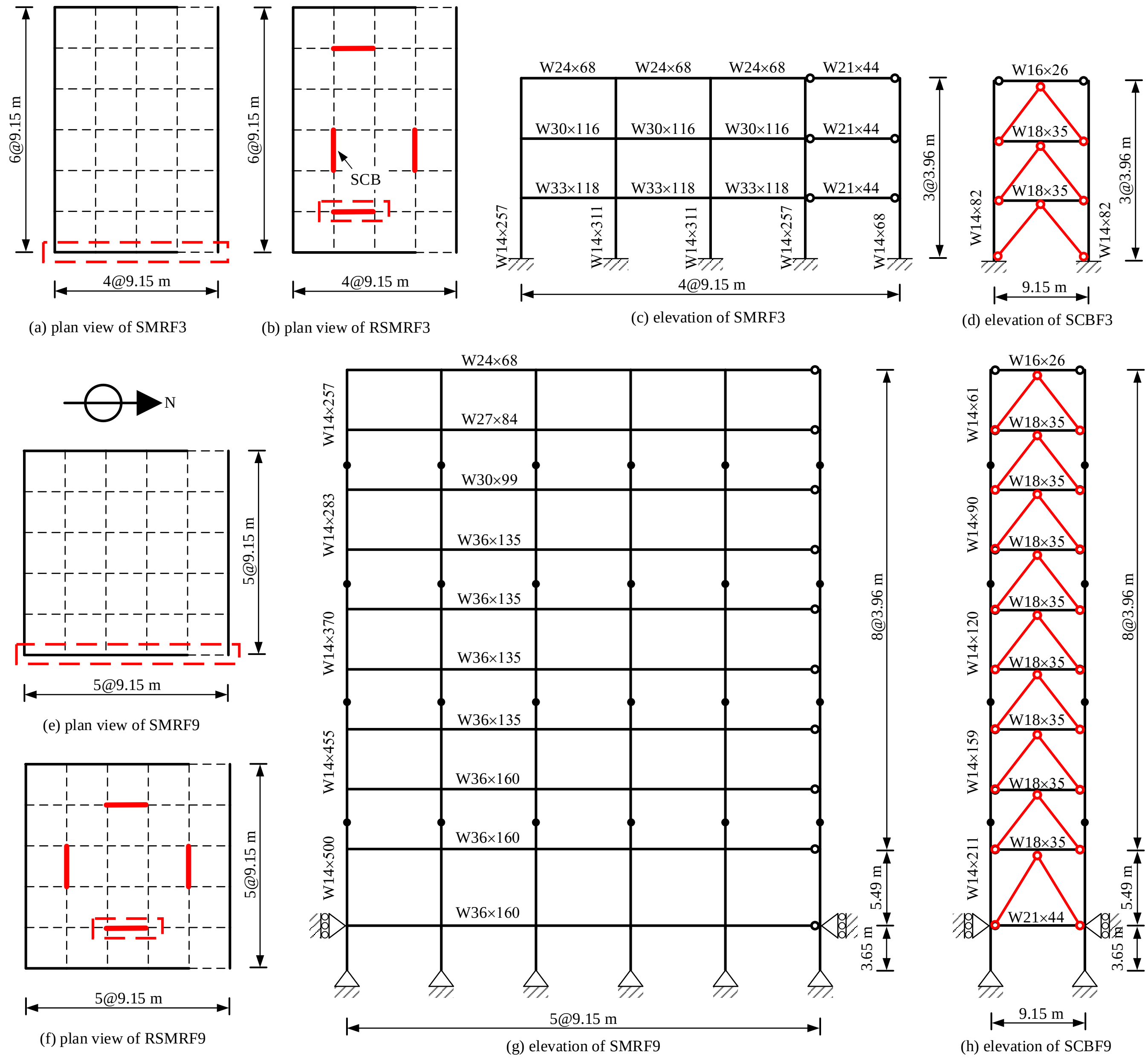

Fig. 7. Plan views and elevations of considered systems.

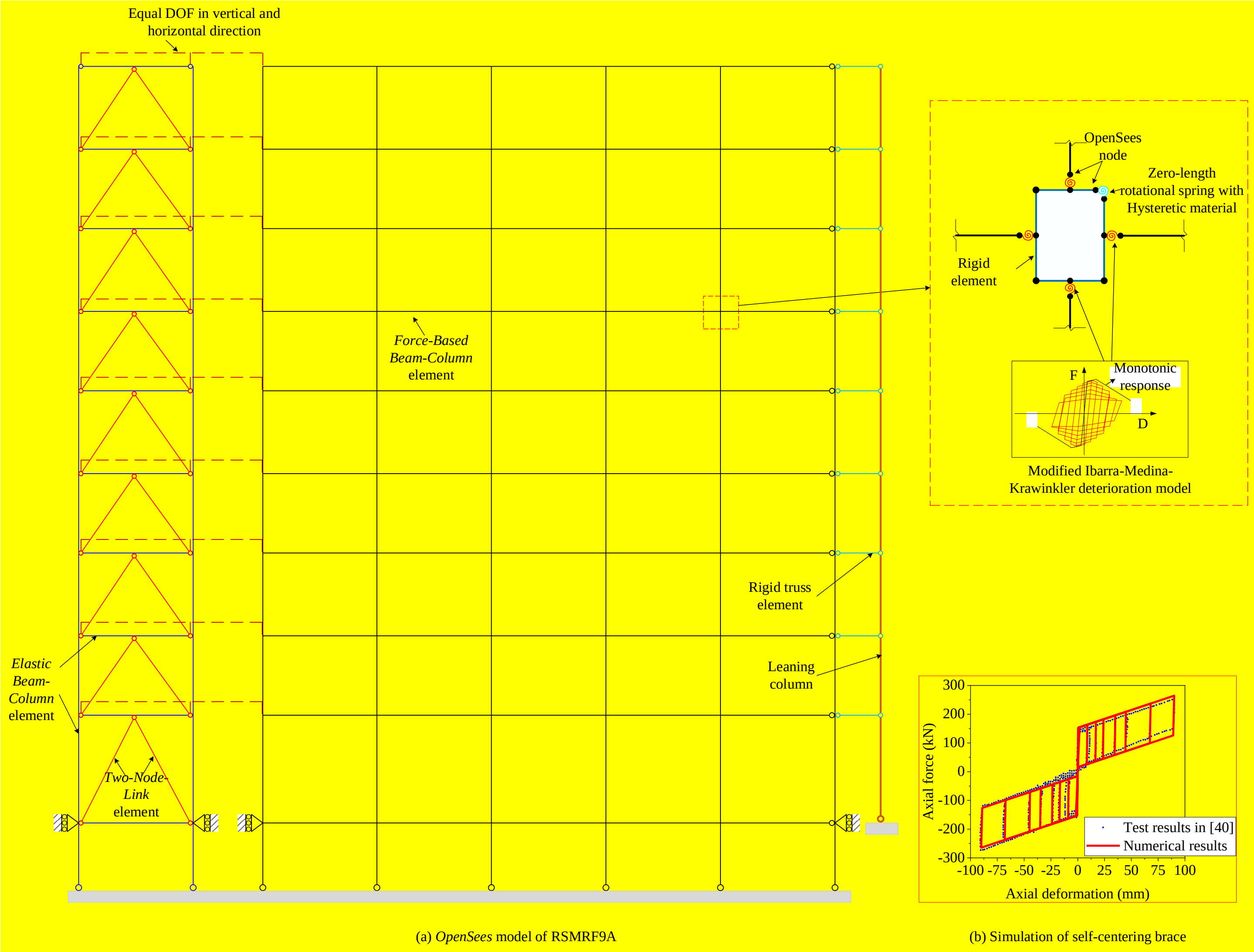

Fig. 8. *OpenSees* model of RSMRF9A.

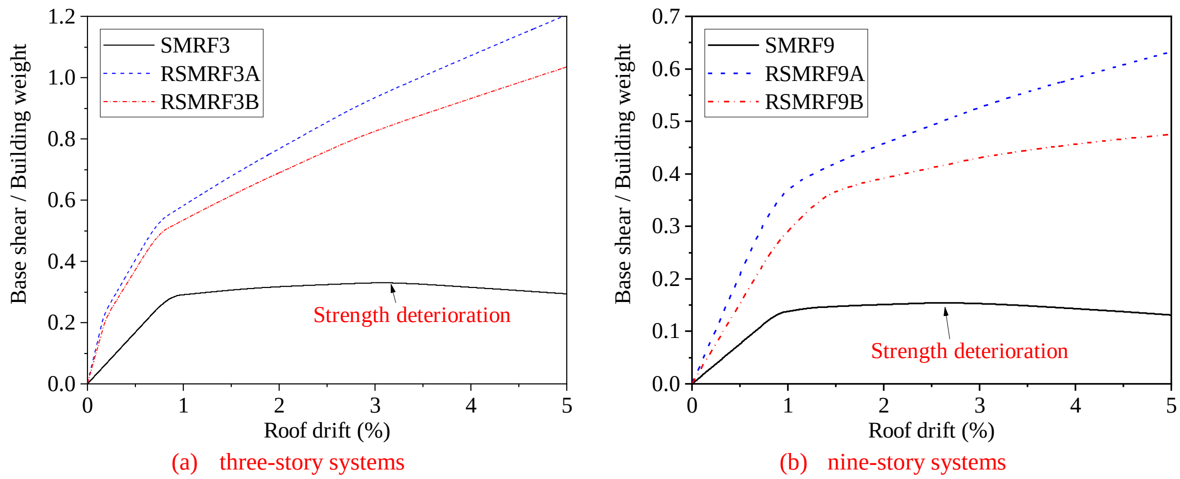

Fig. 9. Static nonlinear behavior of considered systems.

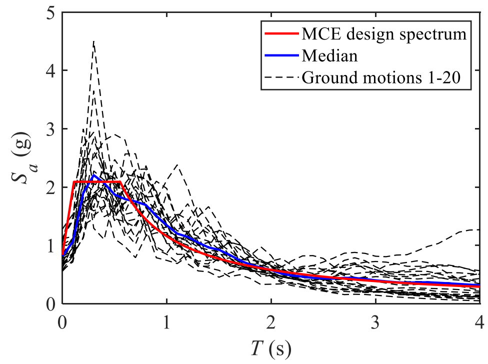

Fig. 10. Spectral accelerations of selected ground motions.

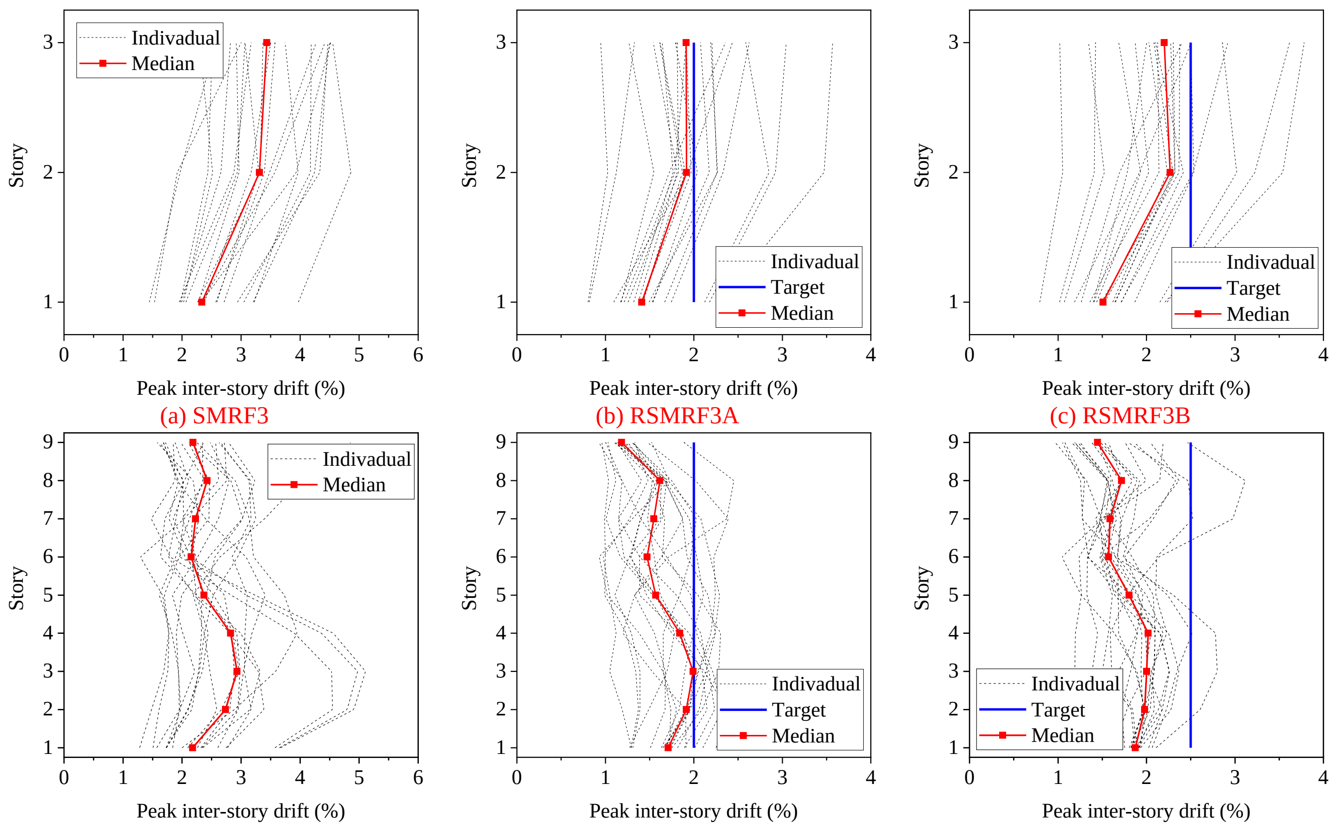

Fig. 11. Peak inter-story drift responses of the considered systems under MCE.

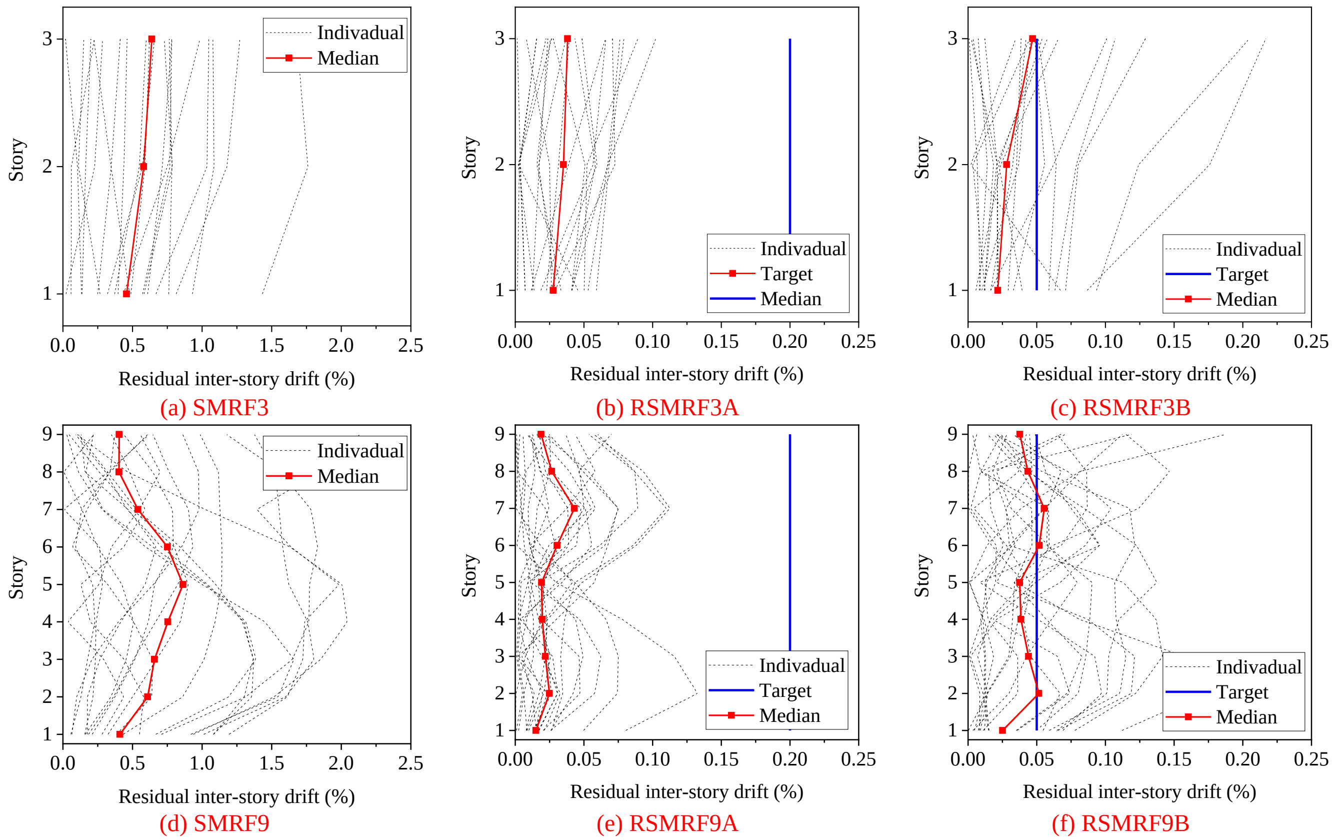

Fig. 12. Residual inter-story drift responses of the considered systems under MCE.